Formatted: Numbering: Continuous

Mercury's Field-aligned Currents: Perspectives from Hybrid Simulations

Z. Shi[1, 2], Z. J. Rong[1, 2, 3], S. Fatemi[4], C. F. Dong[5], Lucy Klinger[6], J. W. Gao[1, 2], J. A. Slavin[7], F. He[1, 2, 3], Y. Wei[1, 2, 3], M. Holmström[8], and S. Barabash[8]

[1]Key Laboratory of Earth and Planetary Physics, Institute of Geology and Geophysics, Chinese Academy of Sciences, Beijing 100029, China.

[2]College of Earth and Planetary Sciences, University of Chinese Academy of Sciences, Beijing, China.

[3]Mohe Observatory of Geophysics, Institute of Geology and Geophysics, Chinese Academy of Sciences, Beijing, China.

[4]Department of Physics at Umeå University, Umeå, Sweden.

[5]Center for Space Physics and Department of Astronomy, Boston University, Boston, MA, USA.

[6]Beijing International Center for Mathematical Research, Peking University, Beijing, China

[7]Department of Climate and Space Sciences and Engineering, University of Michigan, Ann Arbor, MI, USA

[8]Swedish Institute of Space Physics, Kiruna, Sweden

Corresponding author: Z. J. Rong (rongzhaojin@mail.iggcas.ac.cn)

Key Points:

- The field-aligned currents including the types of region 1-like, region 2-like, and NBZ-like are reproduced in our simulations.
- The effective interior conductance required to close the field-aligned currents could be about 2.4-3.4 S.
- The modulations of current patterns by IMF are similar to those of the terrestrial magnetosphere, except for the region 2-like currents.

Abstract

Previous studies suggested that Mercury's terrestrial-like magnetosphere could possess Earth-like field-aligned currents (FACs) despite having no ionosphere. However, due to the limited coverage of spacecraft observations, our knowledge about Mercury's FACs is scarce. Here, to survey the establishment and global pattern of Mercury's FACs, we used Amitis, a hybrid-kinetic plasma model, to simulate the response of Mercury's FACs to different interior conductivity profiles and various orientations of the upstream interplanetary magnetic field (IMF). We find that the planet with a conductive interior favors the establishment of FACs, and that IMF orientation controls the pattern of FACs in a similar manner as it does on Earth. But the response of R2-like FACs to IMF orientation differs, thus we cannot simply regard Mercury's FACs as a scaled-down version of Earth's. Comparison between our simulations and the previous data analysis suggests that the effective interior conductance to close Mercury's FACs is ~2.4-3.4 S.

Plain Language Summary

Studies on the terrestrial magnetosphere suggest that the closure of magnetospheric field-aligned currents (FACs) which flow along the magnetic field requires an ionosphere. Since Mercury has no atmosphere and ionosphere, we would expect that its magnetosphere has no FACs. Nevertheless, previous studies have demonstrated that Mercury could also possess FACs which are closed via Mercury's large conductive interior. Given the existence of Mercury's FACs, we still know little about their establishment and how they respond to different upstream solar wind conditions. In this paper, we use a hybrid plasma model, to demonstrate that Mercury's interior conductivity profile could be the key to determining the establishment of FACs and how the upstream IMF orientation modulates their distribution pattern.

1 Introduction

Mercury and Earth are the only two terrestrial planets with global intrinsic magnetic fields in our solar system [Ness et al., 1974]. Compared to Earth, Mercury's dipole is much weaker (dipole moment is ~195 ± 10 nT R_M^3, where R_M is Mercury's radius which equals $2{,}440\ km$). The dipole is orientated southward (tilt angle < 3°) and its center is shifted northward by ~484 ± 11 km ($\approx 0.2\ R_M$) [Anderson et al., 2011]. Since Mercury is the closest planet to the Sun, it encounters solar wind with a density ~10 times higher than Earth, and its interplanetary magnetic field (IMF) magnitude is ~5 times stronger than that observed in Earth's orbit [Korth et al., 2011]. Consequently, the interaction between the weaker planetary magnetic field and the more robust solar wind gives rise to a very dynamic and smaller magnetosphere (scale is ~5% of the terrestrial magnetosphere [Winslow et al., 2013]). Besides, Mercury has a tenuous exosphere and no ionosphere [Broadfoot et al., 1974; Potter & Morgan, 1985]. And interestingly, Mercury's core is really large (the core's radius, $R_C \sim 0.8\ R_M$) and electrically conductive [Genova et al., 2019; Hauck et al., 2013].

In the terrestrial magnetosphere, "field-aligned currents (FACs)" or "Birkeland currents" [Birkeland, 1908] are typically magnetospheric currents flowing downward along the magnetic field lines into the ionosphere or outward from it. FACs play an important role in coupling solar

wind, the magnetosphere, and the ionosphere [Anderson et al., 2008, 2018; Korth et al., 2010]. Large-scale FACs can be classified into two types [Iijima and Potemra, 1976]: region 1 (R1) and region 2 (R2). The R1 FACs are located in the poleward oval-like region with currents flowing into (outward from) the ionosphere at dawn (dusk) side. The R2 FACs are located equatorward of R1 FACs, and their current directions are opposite to that of R1 FACs. Another type of FACs, NBZ, was found afterward by Iijima et al. [1984]. NBZ FACs appear when the northward IMF is strong. NBZ FACs are located poleward of R1 FACs and their currents flow in the opposite direction to those of R1 FACs. Ionospheric Hall and Pederson conductivities are responsible for the closure of these FACs [Anderson et al., 2018].

Does Mercury's weak magnetosphere possess FACs though Mercury has no ionosphere [Broadfoot et al., 1974; Potter & Morgan, 1985]? By examining the flyby measurements of Mariner 10, Slavin et al. [1997] presented evidence of FACs' signature by detecting a change in magnetic field direction. Based on a statistical survey of orbital magnetic field measurements of MESSENGER (Mercury Surface, Space Environment, GEochemistry, and Ranging), Anderson et al. [2014] demonstrated the existence of steady-state R1-like FACs and Stephens & Korth [2024] derived an empirical model for these R1-like FACs. Recently, Aizawa et al. [2023] argued that an inverted-V signature of the electron spectrum detected by BepiColombo on the dawn side could be induced by R2-like FACs. Mercury's FACs are also successfully reproduced by various simulation models (e.g., MHD model [Ip & Kopp, 2004], hybrid model [Janhunen & Kallio, 2004; Exner et al., 2020], and ten-moment multifluid model [Dong et al., 2019]).

Given the existence of FACs, how do those FACs complete the closure without a fully conducting ionosphere? Before MESSENGER mission, considering the conductance of Mercury's tenuous exosphere (~ 0.1 S) [Cheng et al., 1987], Ip & Kopp [2004] argued that a possible partially conducting ionosphere could support Mercury's FACs. Glassmeier [1997] considered the possibility of FACs' closure near the planet's surface via the low conductance of the regolith. Inspired by that work, Janhunen &Kallio [2004] proposed a two-layer model of interior conductivity profile which consists of a resistive upper layer and a semi-infinite conductive lower layer. According to MESSENGER's observations, Anderson et al. [2014, 2018] found Mercury has steady-state R1 FACs and the effective conductance for FACs' closure is ~ 1 S. Since the exosphere and regolith cannot provide enough conductance, Anderson et al. [2014, 2018] support the two-layer model. And the two-layer model has been used in various simulations [Dong et al., 2019; Exner et al., 2020; Guo et al., 2024]. However, the impact of Mercury's interior conductivity profile on the closure of FACs remains unclear. Furthermore, how IMF orientation affects the pattern of FACs has been extensively studied in the terrestrial magnetosphere. For instance, IMF B_x causes a north-south asymmetry [Reistad et al., 2014], IMF B_y causes a dawn-dusk asymmetry [Tenfjord et al., 2015], and IMF B_z regulates the intensity of FACs [Anderson et al., 2008; Korth et al., 2010]. But at Mercury, the influence of IMF orientation on Mercury's FACs has not been studied.

In this paper, we use a 3D hybrid model to study in detail how Mercury's FACs are controlled by Mercury's conductivity profile and IMF orientation. The influences of other solar wind properties (e.g., the IMF magnitude, and dynamic pressure) are not addressed here. This paper is organized as follows: the hybrid model, initializations, and the current calculation are explained in Section 2. We show the simulation results in Section 3. We end with our discussion and conclusion in Section 4.

2 Model and Methodology

2.1 Model Initialization

In this study we used Amitis, a 3D (in both configuration and velocity space), time-dependent hybrid plasma model (where ions are macroparticles and electrons are a mass-less charge-neutralizing fluid) that runs in parallel on Graphics Processing Units (GPUs) [Fatemi et al., 2017; Fatemi et al., 2022]. This model has been applied successfully to study the plasma environment around various celestial bodies, including Mercury, Mars, Ganymede, Moon, and asteroids [e.g., Aizawa et al., 2021; Fatemi & Poppe, 2018; Fatemi et al., 2018, 2020, 2022; Fuqua-Haviland et al., 2019; Poppe & Fatemi, 2023; Shi et al., 2022; Wang et al., 2023]. In Amitis, the Lorentz equation of motion is applied to advance particle trajectories in time,

$$\frac{d\mathbf{v}_i}{dt} = \frac{q_i}{m_i}(\mathbf{E} + \mathbf{v}_i \times \mathbf{B}), \qquad \frac{d\mathbf{r}_i}{dt} = \mathbf{v}_i \ \#(1)$$

where $\mathbf{r}_i$, $\mathbf{v}_i$, q_i are the position, velocity, and charge of the ion, and $\mathbf{E}$ and $\mathbf{B}$ are the electric field and the magnetic field, respectively. The electric field is derived from the momentum equation for mass-less electrons ($m_e = 0$):

$$\mathbf{E} = \overbrace{(-\mathbf{u}_i \times \mathbf{B})}^{\text{Convective}} + \overbrace{\mathbf{J} \times \mathbf{B}/\rho_i}^{Hall} + \overbrace{\eta \mathbf{J}}^{Ohmic} - \overbrace{\nabla P_e/\rho_i}^{Ambipolar} \ \#(2)$$

where $\mathbf{u}_i$ and ρ_i are the bulk flow velocity and charge density of macroparticle ions, respectively. $\mathbf{J}$ is the current density calculated by Ampère's law ($\mathbf{J} = \nabla \times \mathbf{B}/\mu_0$), η is the resistivity, and P_e is the electron pressure. The four electric field terms on the right side of Equation (2) are convective or motional, Hall, ohmic, and ambipolar, respectively. The magnetic field is advanced in time via Faraday's law ($\partial \mathbf{B}/\partial t = -\nabla \times \mathbf{E}$).

The simulations are conducted in Mercury Solar Orbital (MSO) orthogonal coordinate: the origin is at the planet's center, the +x-axis points to the Sun, the +z-axis points to the north, and the +y-axis completes the right-hand coordinate system. The size of the simulation domain along each axis is described in Table 1. We used cubic grid cells of size 100 km. Mercury's dipole, pointing towards the -z-direction, is placed 484 km northward from the origin. The ions in the solar wind are assumed to be protons only with the properties listed in Table 1.

Table 1. Initial parameters.

Parameter								Value
Coordinate system								MSO
Simulation domain	X range							~ [-6.6, 9.0] R_M
	Y range							~ [-11.5, 11.5] R_M
	Z range							~ [-11.5, 11.5] R_M
Grid size (km)								100
Mercury's radius, R_M (km)								2,440
Core radius, R_C (km)								2,000
Plasma Conductivity (S/m)								10^{-4}
Vacuum Conductivity (S/m)								2×10^{-7}
Time (s)	Time step							5×10^{-4}
	Total simulation time							150
Mercury's dipole moment (A m^2)								2.7×10^{19}
Northward offset of the dipole center (km)								484
Upstream Plasma	Ion species							H^+
	Ion number density (#/cm^3)							30
	Ion temperature (K)							1.4×10^5
	Particle per cell							9
	Electron temperature (K)							1.4×10^5
	Bulk velocity (km/s)	V_x						-370
		V_y						0
		V_z						0
Upstream IMF (nT)	Case[1]		C1	C2	C3	C4	C5	C6
	B_x		17.0	17.0	-17.0	-17.0	17.0	17.0
	B_y		0	0	0	0	6.0	-6.0
	B_z		6.0	-6.0	6.0	-6.0	0	0
Mercury's Conductivity (S/m)	Conductivity profile[2]		RP		RC		LC	
	Core (σ_c)		2×10^{-7}		1,000		1,000	
	Upper layer[3] (σ_u)		2×10^{-7}		2×10^{-7}		2×10^{-6}	

[1]: The simulations are categorized into six cases according to the upstream IMF setting, which are coded as C1 to C6, respectively.

[2]: There are three sets of interior conductivity profiles: a resistive planet (RP), a resistivity upper layer with a conductive core (RC) and a less resistive upper layer with a conductive core (LC).

2.2 The Conductivity Profile and IMF Condition

To investigate the influence of the interior conductivity profile and IMF orientation, we ran 14 cases, which simulate three different conductivity profiles under six varying IMF conditions (Table 1). The three conductivity profiles are a resistive planet (RP), a resistivity upper layer with a conductive core (RC), and a less resistive upper layer with a conductive core (LC). We ran two cases to test the effects of RP profile. RC and LC profiles are set to test the two-layer model. The upper layer is comprised of the crust and mantle, and the lower layer is the core. To examine the influence of IMF orientation, we ran six cases under different IMF orientations (labeled as C1 to C6 in Table 1) for each two-layer model profile. Thus, in total, we have 14 cases: $[\mathrm{RP}] \times [\mathrm{C1}, \mathrm{C2}] + [\mathrm{RC}, \mathrm{LC}] \times [\mathrm{C1} - \mathrm{C6}]$.

2.3 Calculations of Currents and Conductance

The parallel component of the current density, $J_\parallel$, is obtained by $J_\parallel = \mathbf{B} \cdot \mathbf{J}/|\mathbf{B}|$. To calculate the total current (I) of a specific FAC branch, we need to know the cross-section (S) where the branch intersects the planetary surface. Considering the continuity and connectivity of the currents inside a branch, a 3D treatment is used to derive the cross-section (Text S1). Then the total current carried by one branch can be derived by integrating **J** across the cross-section, that is, $I = \iint_S \mathbf{J} \cdot \mathrm{d}\mathbf{s}$.

Once the polar cap electric potential (U_{drop}) is obtained, the effective conductance (Σ, the conductance the planet provided to close the FACs) can be derived by $\Sigma = I/U_{drop}$. The procedure is as follows. First, we arbitrarily set the electric potential (U) at the point, **O** ($X_{mso} = -1.2\ R_M$, $Y_{mso} = -1.2\ R_M$, $Z_{mso} = -1.2\ R_M$), as zero and then derive U at each grid point by integrating **E** along an arbitrary simple curve (l) from **O** to the grid point ($U = \int_l \mathbf{E} \cdot \mathrm{d}\mathbf{l}$). Then, based on the derived distribution of U at the surface of the planet, we can find the highest (lowest) U in the inward (outward) branch of the concerned FACs, U_h (U_l) and calculate the U_{drop} ($U_{drop} = U_h - U_l$). Finally, we calculate the total current of the concerned FACs by $I = \iint_S \mathbf{J} \cdot \mathrm{d}\mathbf{s}$ and derive the effective conductance using $\Sigma = I/U_{drop}$. Our main interest here are the quantitative descriptions of R1-like FACs, which will be detailed in the following section.

3 Results

3.1 Overall Distributions

The distributions of $|J_\parallel|$ from all the 14 simulated cases are shown in Figure 1. Note that, instead of the polarity of $J_\parallel$, $J_\parallel$ is colored according to its direction inwards or outwards regarding the planet. To be succinct, the three types of FACs that appeared in simulations (see Figure 1d) could be referred to as R1-like, R2-like, and NBZ-like FACs, respectively, after their counterparts on Earth [Iijima & Potemra, 1976; Iijima et al., 1984]. Among these three types, the R1-like FAC, which flows inwards at dawn side and upwards at dusk side, is the only type that has been observed by MESSENGER [Anderson et al., 2014, 2018]. And as is evident in Figure 1, it is the most significant, particularly in the case of the LC profile. Thus, we focused solely on the calculations of R1-like FACs from the simulations. To compare simulations with observations, we calculated the total currents, I_{R1}, of the R1-like FACs (Table 2). From the electric potential distributions (Figure S2), we derived the potential drops between the two branches of the R1-like FACs, $U_{drop,R1}$ (Table 2). Then, the effective conductance, Σ_{R1}, of each case can be calculated as $\Sigma_{R1} = I_{R1}/U_{drop,R1}$. From Figure 1, we see that FACs occupy a larger area in the southern hemisphere. While the equatorward edge of the R1-like FACs extends to ~50°N in the northern hemisphere, it can extend to ~30°S in the southern hemisphere. This hemispheric asymmetry is associated with the northward shift of the dipole center.

Table 2 summarizes how R1-like FACs respond to different interior conductivity profiles and IMF orientations. Here, we find that the calculated Σ_{R1} in the southern hemisphere is larger (the larger cross-section could result in higher conductance according to Pouillet's law). The $U_{drop,R1}$ from both hemispheres are nearly the same, so it is reasonable to find a stronger I_{R1} (Table 2) and a slightly weaker $|J_\parallel|$ (Table S1) in the southern hemisphere.

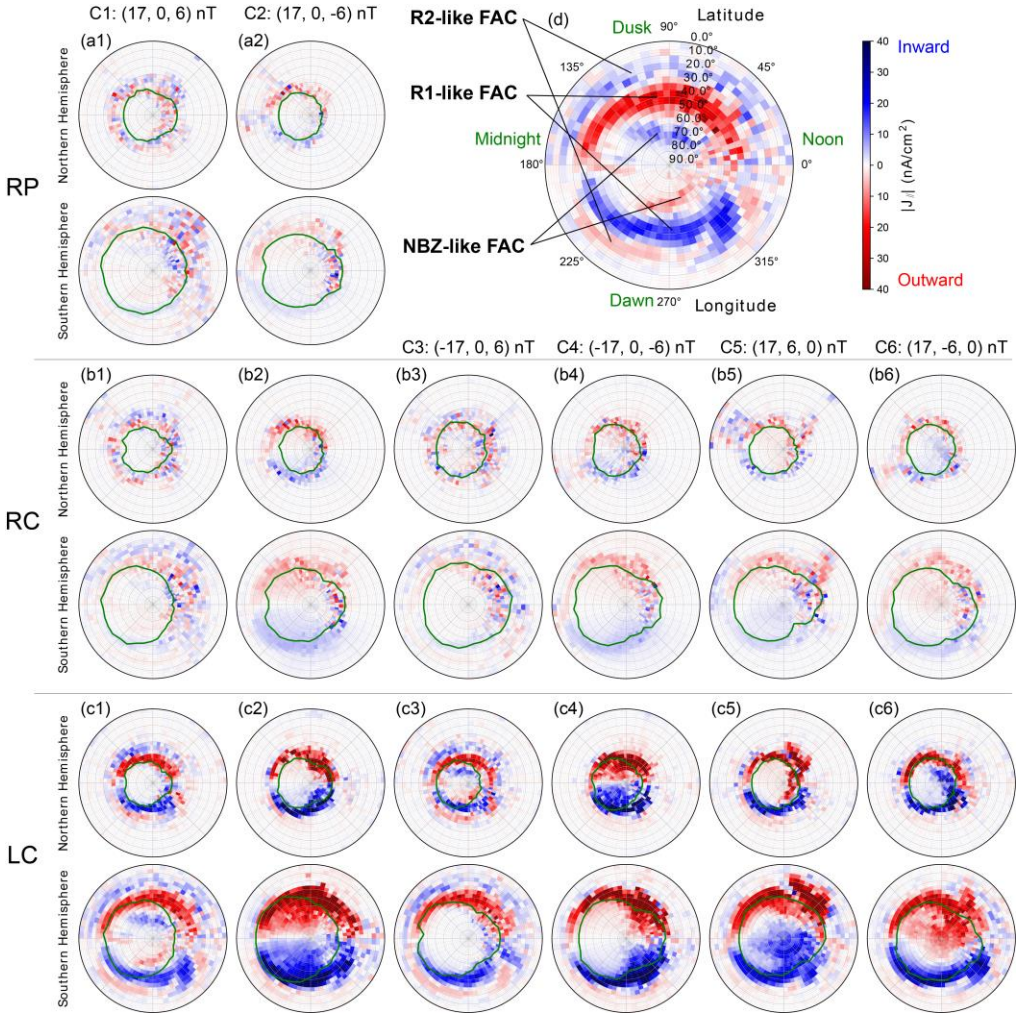

Figure 1. Spatial distributions of $|J_{\parallel}|$ under different upstream IMF orientations and conductivity profiles. Each case shows two polar maps corresponding to both hemispheres. Green circles denote the open/closed magnetic field line boundary, which was identified in our model for each case. Panel (d), which is the zoomed-in plot of the panel (c1) in the southern hemisphere, shows a reference format for the coordinate system and colormap. The three types of FACs (the R1-like, R2-like and NBZ-like) are indicated respectively in panel (d).

Table 2. Calculated parameters, including total current, electric potential, and effective conductance, associated with R1-like FACs.

Case	Conductivity Profile	The North Hemisphere			The South Hemisphere		
		I_{R1} (kA)[1]	$U_{drop,\ R1}$ (kV)[2]	Σ_{R1} (S)[3]	I_{R1} (kA)	$U_{drop,\ R1}$ (kV)	Σ_{R1} (S)
C1 (IMF = [17, 0, 6] nT)	**LC**	27.03	11.34	2.38	63.54	11.68	4.28
	RC	4.65	-[4]	-	3.06	-	-
	RP	-	-	-	-	-	-
C2 (IMF = [17, 0, −6] nT)	**LC**	63.54	22.10	2.87	171.36	22.32	7.68
	RC	11.00	28.83	0.38	20.44	27.90	0.73
	RP	5.28	27.21	0.19	3.67	-	-
C3 (IMF = [−17, 0, 6] nT)	**LC**	27.54	10.99	2.51	49.90	10.52	4.74
	RC	3.50	-	-	2.41	-	-
C4 (IMF = [−17, 0, −6] nT)	**LC**	82.78	24.28	3.41	128.36	25.73	4.99
	RC	8.9	26.59	0.33	14.89	27.62	0.54
C5 (IMF = [17, 6, 0] nT)	**LC**	58.71	24.88	2.36	131.40	24.84	5.29
	RC	5.41	19.11	0.28	8.82	19.74	0.45
C6 (IMF = [17, −6, 0] nT)	**LC**	57.70	17.07	3.38	113.96	16.59	6.87
	RC	7.10	18.20	0.39	8.87	18.47	0.48

[1]: Total current of R1-like FACs (I_{R1}), which is the mean of the current carried by the two branches of FACs.

[2]: Electric potential drop (U_{R1}).

[3]: Effective conductance (Σ_{R1}).

[4]: We cannot determine the specific value when the current density is too weak to be used in identifying the pattern of R1-like FACs or only one branch of the R1-like FACs can be identified (Text S1).

3.1.1 The effect of the conductivity profile

From Figure 1, we see that Mercury's FACs in both hemispheres become more significant as the interior conductivity increases from RP to RC and then to LC. Moreover, I_{R1}, Σ_{R1} and $|J_{\parallel}|$ increase as the conductivity increases (Table 2 and Table S1). For the RP profile, when the IMF is northward (C1), the dayside reconnection rate is low [Milan et al., 2012], and therefore large-scale FACs are not well established (Figure 1 (a1)). In contrast, when IMF is southward, the reconnection rate is high [Milan et al., 2012], and faint large-scale R1-like FACs form (Figure 1 (a2)). Unlike the RP profile, the RC profile, with a conductive core inside, allows weak large-scale FACs to form (Figure 1 (b1-b6)). When the upper layer becomes less resistive (LC), FACs are well established (Figure 1 (c1-c6)). In this case, Σ_{R1} in the northern hemisphere is ~2.4-3.4 S, which is in the same order as that estimated by Anderson et al. [2014].

Since simulated FACs are most significant when the LC profile is adopted, in the following sections we focus on the IMF effects on FACs for the LC profile (i.e., panels c1-c6 in Figure 1).

3.1.2 The effect of the IMF B_x polarity

The IMF B_x could affect the north-south asymmetries of FACs. There are two aspects involved in this affection. When IMF is northward, NBZ-like FACs show up (Figure 1 (c1 and c3)) within the open/closed field line boundary. The NBZ-like FACs appear in the southern (northern) hemisphere when IMF is sunward (anti-sunward). In terrestrial studies, the appearance of NBZ FACs is related to four-cell-like convection in the polar cap under northward IMF, as well as to the reconnection between IMF and the lobe field (Erlandson et al., 1988; Maezawa, 1976). The polarity of IMF B_x can affect the reconnection site, which could explain regulating the hemispheric bias of NBZ-like FACs.

In addition, when IMF is southward, the R1-like FACs are enhanced in the southern (northern) hemisphere if IMF is sunward (anti-sunward): the intensity of R1-like FACs is higher (Table S1), and its spatial coverage becomes wider (Figure 1 (c2 and c4)). Studies of terrestrial FACs suggest that similar phenomena are caused by the regulation of IMF B_x, which influences the efficiency of the solar wind dynamo. Specifically, the polarity of IMF B_x affects the north-south asymmetry of the tension force on the newly opened field lines in both hemispheres. This leads to higher efficiency of the solar wind dynamo in the southern (northern) hemisphere when IMF is sunward (anti-sunward). And the difference in the dynamo efficiency is reflected in the north-south asymmetry of the R1 FACs (Reistad et al., 2014).

3.1.3 The effect of the IMF B_y polarity

Our simulations show that the IMF B_y affects dawn-dusk asymmetries of FACs. When IMF B_y is positive (Figure 1 (c5)), the outward branch of R1-like FACs in the northern hemisphere (red) extends to the dayside polar cap and across the noon-night meridian to the dawn side. In the southern hemisphere, the outward branch (red) is basically located at the dusk side, but the inward branch (blue) extends to the dusk side and nearly fills the polar cap. When the IMF B_y is negative (Figure 1 (c6)), the R1-like FACs present opposing patterns to those under positive IMF B_y. An analogous dawn-dusk asymmetry of FACs induced by IMF B_y has also been investigated in the terrestrial magnetosphere [Anderson et al., 2008]. Tenfjord et al. [2015] demonstrated that IMF B_y induces an uneven distribution of tension force and magnetic flux in the magnetosphere. This leads to the observed asymmetry.

3.1.4 The effect of the IMF B_z polarity

IMF B_z could affect the intensity of R1-like FACs and control the appearance of R2-like and NBZ-like FACs. When the IMF is southward, the R1-like FACs are generally enhanced (comparing Figure 1 (c1 and c2) or Figure 1 (c3 and c4)). A similar effect of IMF B_z on terrestrial FACs has been observed previously, which might be due to the dayside reconnection rate being positively related to $\sin\theta/2$ (where θ is the IMF's clock angle): the more southward the IMF, the larger the dayside reconnection rate [Anderson et al., 2008; Milan et al., 2012]. Besides, reconnection at Mercury is more intense and could occur when IMF has a small shear angle relative to the planetary field [DiBraccio et al., 2013]. Thus, compared to the northward IMF, the appearance of IMF B_y can enhance FACs (Figure 1 (c5 and c6)).

When IMF is northward, the R2-like FACs appear in both hemispheres while NBZ-like FACs only appear in one hemisphere depending on the IMF B_x polarity (comparing Figure 1 (c1 and c2) or Figure 1 (c3 and c4)). However, the R2 FACs in the terrestrial magnetosphere are

stronger when the IMF is southward [Anderson et al., 2008], which is different from the results presented here. This discrepancy might be due to the closure of terrestrial R2 FACs and its relation to the partial ring current. For Mercury, the establishment of its R2-like FACs may relate to the night side plasma belt, which is more evident when IMF is northward [Shi et al., 2022, 2023].

3.2 Closure of R1-like FACs

Distributions of $J_{\parallel}$ for all the cases are shown in Figure 2. In cases with the RP profile, FACs are weak (Figure 2 (c1 and c2)). If the core is more conductive (RC), FACs are slightly stronger (Figure 1 (b1-b6)). If we make the upper layer less resistive (LC profile), R1-like FACs are well established (Figure 2 (a1-a6)). R1-like FACs flow into the planet on the dawn side, penetrate the upper layer, and reach the core surface; then, the currents flow laterally to the dusk side of the conductive core surface and out of the upper layer on the dusk side as the outward branches. This is in agreement with the current closure described earlier by Janhunen & Kalio [2004] and Anderson et al. [2014, 2018]. To clarify this picture more clearly, a schematic diagram is shown in Figure 2 (d).

The closure of the R1-like FACs with magnetospheric currents is also examined by tracing the average current lines (Figure S3). We find that when the IMF is northward, part of the R1-like FACs connect to the magnetopause currents directly, and part of it connects to the cross-tail current in the plasma sheet near the low-latitude boundary layer (Figure S3 (a and c)). In addition, when the IMF is southward, part of the R1-like FACs could connect to the cross-tail current near midnight, like a substorm current wedge [Dewey et al., 2020] (Figure S3 (b and d)).

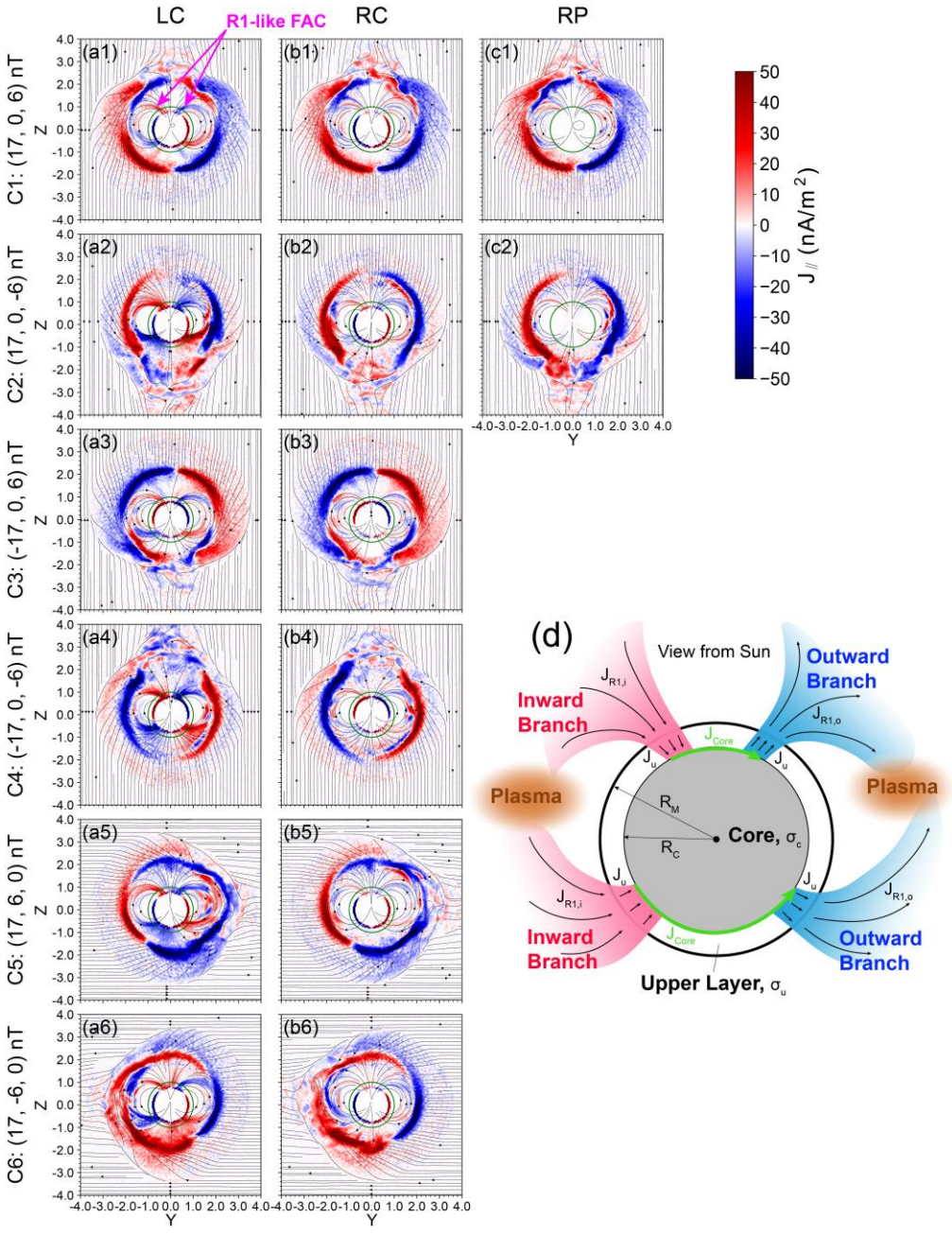

Figure 2. Distributions of $J_{\parallel}$ in YZ plane with $|x| < 0.15\,R_M$ for all simulated cases (a1-c2) where the bin size in each plot is 100×100 km. The average magnetic field lines are shown by

black streamlines. The surface of Mercury is marked by a green circle. A diagram of R1-like FACs with LC profile is displayed in panel (d), where the gray circle is the core and the thick black circle represents Mercury's surface. Pink patches represent inward branches ($J_{R1,i}$), while blue patches represent outward branches ($J_{R1,o}$); current lines around patches are indicated by thin black lines. J_u is the current inside the upper layer, and J_{Core} (green arrows) is the current across the core's surface. Brown ellipses represent the plasma of magnetospheric sources near magnetic equator.

Discussion and Conclusion

In this study, we used a hybrid model to investigate how Mercury's FACs are affected by the interior conductivity profile and the orientation of the upstream IMF. Our discussion and conclusion are summarized as follows:

1. FACs can be well established when the upper layer of Mercury's interior is less resistive and the core is highly conductive (see the cases with LC in Section 3.1.1). For R1-like FACs, simulated cases with LC demonstrated that the estimated I_{R1}, U_{R1}, and Σ_{R1} are ~30-80 kA, ~10-25 kV, and ~2.4-3.4 S, respectively. The maximum and the mean of simulated $|J_{\parallel}|$ are ~30-100 nA/m^2 and ~10-20 nA/m^2. Our simulation results are in agreement with earlier observations [Anderson et al.,2014,2018]. The statistical survey of Anderson et al. [2014] found that the typical current intensity, electric potential drop, and effective conductance of their found FACs (R1-like) are 20-40 kA, ~30 kV, and ~1 S, respectively, and the typical current density is 10-30 nA/m^2 with a maximum of up to 115 nA/m^2. Given a typical solar wind electric potential drop (~10-30 kV) as applied to the magnetosphere [Blomberg et al., 2006; DiBraccio et al., 2013; Slavin et al., 2009] and the range of total currents of FACs (~20-60 kA) over different activity levels [Anderson et al., 2018], the effective conductance of FACs could be estimated as ~2 S.
2. Our simulations suggest that the regulation of Mercury's FACs by the IMF orientation performs similarly to that found in terrestrial FACs: the IMF B_x mainly regulates the north-south asymmetries of FACs, the IMF B_y mainly regulates the dawn-dusk asymmetries of FACs, and the IMF B_z regulates the intensity of the R1-like FACs. Based on our simulations, R1-like FACs are predominant and their intensity and spatial coverage are much larger than other types of FACs. Given the IMF properties around Mercury (less probability for the occurrence of positive IMF B_z) [James et al., 2017], the statistically yielded pattern of FACs (R1-like) by Anderson et al. [2014] is consistent with our simulation results. Note that, although Anderson et al. [2018] categorized the response of FACs according to the magnetic disturbance index, the influence of the IMF orientation cannot be ruled out in their study, mainly due to the lack of an upstream observer.
3. Both R2-like FACs and NBZ-like FACs also appear in our simulations. Recently, Aizawa et al. [2023] reported that R2-like FACs may exist in Mercury's magnetosphere. From our study, however, R2-like FACs responses to the IMF B_z are the opposite to those found in the terrestrial magnetosphere: Mercury's R2-like FACs would become weaker when IMF is southward, but, in the terrestrial magnetosphere,

R2 FACs would become stronger (Section 3.1.4). Mercury's R2-like FACs might be connected to the nightside plasma belt [Dewey et al., 2020; Shi et al., 2022, 2023]. That is, the R2-like FACs may connect to the westward current at the outer boundary of the plasma belt, which behaves like the "banana" current in the terrestrial inner magnetosphere [Liemohn et al., 2013]. Therefore, when the IMF is northward, the plasma belt would be significant [Shi et al., 2022, 2023] and the R2-like FACs would become stronger as in our simulations. Although both R2-like FACs and NBZ-like FACs show up in our simulations when the IMF is northward, these types of FACs cannot be identified from the MESSENGER's statistical pattern [Anderson et al., 2014, 2018]. Detailed analysis of the R2 and NBZ FACs will be conducted in a separate study.

In summary, our simulations show that Mercury may have several large-scale FACs: R1-like, R2-like, and NBZ-like FACs. R1-like FACs dominate the whole FACs' pattern. These FACs can be well established when LC profile is present (Σ_{R1}~$2.4-3.4$ S). From our simulations, we also found the regulation of FACs by IMF orientation behaves similarly to ones found in the terrestrial magnetosphere, nonetheless, R2-like FACs' response to IMF is different. Thus, Mercury's magnetosphere is not a simple scaled-down version of Earth's magnetosphere. Note that our present study only focuses on the influences of the interior conductivity profile and IMF orientation. Other factors, like the solar wind dynamic pressure, should be also considered in future studies. Further observational analyses are also needed to study Mercury's FACs, especially with the help of the BepiColombo mission [Milillo et al., 2020].

Acknowledgments

The work was carried out at the National Supercomputer Center in Tianjin, and the calculations were performed on TianHe-1 (A). We also thank the useful discussions with Dr. Maosheng He.

Funding: This work was supported by the Strategic Priority Research Program of Chinese Academy of Sciences (Grant No. XDB 41000000), the National Natural Science Foundation of China (Grant Nos. 41922031, 41774188), the Key Research Program of the Institute of Geology & Geophysics, CAS (Grant Nos. IGGCAS-201904, IGGCAS-202102), and the Key Research Program of Chinese Academy of Sciences (Grant No. ZDBS-SSW-TLC00103). S.F. acknowledges support from the Swedish National Space Agency, Rymdstyrelsen (Grant 2022-00183).

Author contributions: Z.S. contributed to the simulations, data graphics, and prepared the draft of the manuscript. Z.J.R. offered the physical idea and contributed to the draft of the manuscript. S.F. contributed to the simulations and the draft of the manuscript. C.F.D., L.K., J.W.G., J.A.S., F.H., Y.W., M.H. and S.B. contributed to the revision of the manuscript.

Competing interests: Authors declare that they have no competing interests.

References

1. Aizawa, S., Griton, L.S., Fatemi, S., Exner, W., Deca, J., Pantellini, F., et al. (2021). Cross-comparison of global simulation models applied to Mercury's dayside magnetosphere. *Planetary and Space Science*, 198, p.105176.
2. Aizawa, S., André, N., Saito, Y., Rojo, M., Sauvaud, J.A., Fedorov, A., et al. (2023). Electron populations observed by Mercury Electron Analyzer onboard Mio/BepiColombo during its Mercury flybys. *AGU23*. 2023 Dec 14.
3. Anderson, B.J., Korth, H., Waters, C.L., Green, D.L. & Stauning, P. (2008). Statistical Birkeland current distributions from magnetic field observations by the Iridium constellation. In *Annales Geophysicae* (Vol. 26, No. 3, pp. 671-687). Göttingen, Germany: Copernicus Publications.
4. Anderson, B.J., Johnson, C.L., Korth, H., Purucker, M.E., Winslow, R.M., Slavin, J.A., et al. (2011). The global magnetic field of Mercury from MESSENGER orbital observations. *Science*, 333(6051), pp.1859-1862.
5. Anderson, B.J., Johnson, C.L. & Korth, H. (2013). A magnetic disturbance index for Mercury's magnetic field derived from MESSENGER Magnetometer data. *Geochemistry, Geophysics, Geosystems*, 14(9), pp.3875-3886.
6. Anderson, B.J., Johnson, C.L., Korth, H., Slavin, J.A., Winslow, R.M., Phillips, R.J., et al. (2014). Steady-state field-aligned currents at Mercury. *Geophysical Research Letters*, 41(21), pp.7444-7452.
7. Anderson, B.J., Johnson, C.L., Korth, H. & Philpott, L.C. (2018). Birkeland currents at Mercury: Review and comparison with Earth. *Electric currents in geospace and beyond*, pp.279-302.
8. Birkeland, K. (1908). On the cause of magnetic storms and the origin of terrestrial magnetism (No. 1). H. Aschehoug & Company.
9. Blomberg, L.G., Cumnock, J.A., Kasaba, Y., Matsumoto, H., Kojima, H., Omura, et al. (2006). Electric fields in the Hermean environment. *Advances in Space Research*, 38(4), pp.627-631.
10. Broadfoot, A.L., Kumar, S., Belton, M.J.S. & McElroy, M.B. (1974). Mercury's atmosphere from Mariner 10: Preliminary results. *Science*, 185(4146), pp.166-169.
11. Cheng, A.F., Johnson, R.E., Krimigis, S.M. & Lanzerotti, L.J. (1987). Magnetosphere, exosphere, and surface of Mercury. *Icarus*, 71(3), pp.430-440.
12. Dewey, R.M., Slavin, J.A., Raines, J.M., Azari, A.R. & Sun, W. (2020). MESSENGER observations of flow braking and flux pileup of dipolarizations in Mercury's magnetotail: Evidence for current wedge formation. *Journal of Geophysical Research: Space Physics*, 125(9), p.e2020JA028112.
13. DiBraccio, G.A., Slavin, J.A., Boardsen, S.A., Anderson, B.J., Korth, H., Zurbuchen, T.H., et al. (2013). MESSENGER observations of magnetopause structure and dynamics at Mercury. *Journal of Geophysical Research: Space Physics*, 118(3), pp.997-1008.

14. Dong, C., Wang, L., Hakim, A., Bhattacharjee, A., Slavin, J.A., DiBraccio, G.A. & Germaschewski, K. (2019). Global ten-moment multifluid simulations of the solar wind interaction with mercury: From the planetary conducting core to the dynamic magnetosphere. *Geophysical Research Letters*, 46(21), pp.11584-11596.
15. Erlandson, R.E., Zanetti, L.J., Potemra, T.A., Bythrow, P.F. & Lundin, R. (1988). IMF By dependence of region 1 Birkeland currents near noon. *Journal of Geophysical Research: Space Physics*, 93(A9), pp.9804-9814.
16. Exner, W., Simon, S., Heyner, D. & Motschmann, U. (2020). Influence of Mercury's exosphere on the structure of the magnetosphere. *Journal of Geophysical Research: Space Physics*, 125(7), p.e2019JA027691.
17. Fatemi, S., Poppe, A. R., Delory, G. T., & Farrell, W. M. (2017). Amitis: A 3D GPU-based hybrid-PIC model for space and plasma physics journal of physics: Conference series. *IOP Publishing*, 837(1), 012017.
18. Fatemi, S., & Poppe, A. R. (2018). Solar wind plasma interaction with asteroid 16 Psyche: Implication for formation theories. *Geophysical Research Letters*, 45(1), 39-48.
19. Fatemi, S., Poirier, N., Holmström, M., Lindkvist, J., Wieser, M. & Barabash, S. (2018). A modelling approach to infer the solar wind dynamic pressure from magnetic field observations inside Mercury's magnetosphere. *Astronomy & Astrophysics*, 614, p.A132.
20. Fatemi, S., Poppe, A. R., & Barabash, S. (2020). Hybrid simulations of solar wind proton precipitation to the surface of Mercury. *Journal of Geophysical Research: Space Physics*, 125(4), e2019JA027706.
21. Fatemi, S., Poppe, A.R., Vorburger, A., Lindkvist, J. & Hamrin, M. (2022). Ion dynamics at the magnetopause of Ganymede. *Journal of Geophysical Research: Space Physics*, 127(1), p.e2021JA029863.
22. Favorskaya, M.N., Jain, L.C. & Buryachenko, V. (2015). Computer vision in control systems. *Aerial and Satellite Image Processing*, 135.
23. Fuqua Haviland, H., Poppe, A.R., Fatemi, S., Delory, G.T. & De Pater, I., (2019). Time-dependent hybrid plasma simulations of lunar electromagnetic induction in the solar wind. *Geophysical Research Letters*, 46(8), pp.4151-4160.
24. Genova, A., Goossens, S., Mazarico, E., Lemoine, F.G., Neumann, G.A., Kuang, W., et al. (2019). Geodetic evidence that Mercury has a solid inner core. *Geophysical Research Letters*, 46(7), pp.3625-3633.
25. Glassmeier, K.H. (1997). The Hermean magnetosphere and its ionosphere-magnetosphere coupling. *Planetary and space science*, 45(1), pp.119-125.
26. Guo, J., Lu, S., Lu, Q., Slavin, J.A., Sun, W., Ren, J., et al. (2023). Three-Dimensional Global Hybrid Simulations of Mercury's Disappearing Dayside Magnetosphere. *Journal of Geophysical Research: Planets*, 128(12), p.e2023JE008032.
27. Hauck, S.A., Margot, J.L., Solomon, S.C., Phillips, R.J., Johnson, C.L., Lemoine, F.G., et al. (2013). The curious case of Mercury's internal structure. *Journal of Geophysical Research: Planets*, 118(6), pp.1204-1220.

28. Ip, W.H. & Kopp, A. (2004). Mercury's Birkeland current system. *Advances in Space Research*, 33(12), pp.2172-2175.
29. Iijima, T. & Potemra, T.A. (1976). Field-aligned currents in the dayside cusp observed by Triad. *Journal of Geophysical Research*, 81(34), pp.5971-5979.
30. Iijima, T., Potemra, T.A., Zanetti, L.J. & Bythrow, P.F. (1984). Large-scale Birkeland currents in the dayside polar region during strongly northward IMF: A new Birkeland current system. *Journal of Geophysical Research: Space Physics*, 89(A9), pp.7441-7452.
31. James, M.K., Imber, S.M., Bunce, E.J., Yeoman, T.K., Lockwood, M., Owens, M.J. & Slavin, J.A. (2017). Interplanetary magnetic field properties and variability near Mercury's orbit. *Journal of Geophysical Research: Space Physics*, 122(8), pp.7907-7924.
32. Janhunen, P. & Kallio, E. (2004), April. Surface conductivity of Mercury provides current closure and may affect magnetospheric symmetry. In *Annales Geophysicae*, 22(5), 1829-1837. Göttingen, Germany: Copernicus Publications.
33. Korth, H., Anderson, B.J. & Waters, C.L. (2010). Statistical analysis of the dependence of large-scale Birkeland currents on solar wind parameters. In *Annales Geophysicae*, 28(2), pp. 515-530. Göttingen, Germany: Copernicus Publications.
34. Korth, H., Anderson, B.J., Zurbuchen, T.H., Slavin, J.A., Perri, S., Boardsen, S.A., et al. (2011). The interplanetary magnetic field environment at Mercury's orbit. *Planetary and Space Science*, 59(15), pp.2075-2085.
35. Liemohn, M.W., Ganushkina, N.Y., Katus, R.M., De Zeeuw, D.L. & Welling, D.T. (2013). The magnetospheric banana current. *Journal of Geophysical Research: Space Physics*, 118(3), pp.1009-1021.
36. Maezawa, K. (1976). Magnetospheric convection induced by the positive and negative Z components of the interplanetary magnetic field: Quantitative analysis using polar cap magnetic records. *Journal of Geophysical Research*, 81(13), pp.2289-2303.
37. Milillo, A., Fujimoto, M., Murakami, G., Benkhoff, J., Zender, J., Aizawa, S., et al. (2020). Investigating Mercury's environment with the two-spacecraft BepiColombo mission. *Space science reviews*, 216(5), 1-78.
38. Milan, S.E., Gosling, J.S. & Hubert, B. (2012). Relationship between interplanetary parameters and the magnetopause reconnection rate quantified from observations of the expanding polar cap. *Journal of Geophysical Research: Space Physics*, 117(A3).
39. Ness, N.F., Behannon, K.W., Lepping, R.P., Whang, Y.C. & Schatten, K.H. (1974). Magnetic field observations near Mercury: Preliminary results from Mariner 10. *Science*, 185(4146), pp.151-160.
40. Poppe, A.R. and Fatemi, S. (2023). The Solar Wind Interaction with (1) Ceres: The Role of Interior Conductivity. *The Planetary Science Journal*, 4(1), p.14.
41. Potter, A. & Morgan, T. (1985). Discovery of sodium in the atmosphere of Mercury. *Science*, 229(4714), pp.651-653.

42. Reistad, J.P., Østgaard, N., Laundal, K.M., Haaland, S., Tenfjord, P., Snekvik, K., et al. (2014). Intensity asymmetries in the dusk sector of the poleward auroral oval due to IMF Bx. *Journal of Geophysical Research: Space Physics*, 119(12), pp.9497-9507.

43. Shi, Z., Rong, Z.J., Fatemi, S., Slavin, J.A., Klinger, L., Dong, C., et al. (2022). An eastward current encircling Mercury. *Geophysical Research Letters*, 49(10), p.e2022GL098415.

44. Shi, Z., Rong, Z. & Wei, Y. (2023). The plasma belt and the associated current systems in the inner magnetosphere of Mercury. *Chinese Journal of Geophysics*, 66(6), pp.2236-2251.

45. Slavin, J.A., Owen, J.C.J., Connerney, J.E.P. & Christon, S.P. (1997). Mariner 10 observations of field-aligned currents at Mercury. *Planetary and Space Science*, 45(1), pp.133-141.

46. Slavin, J.A., Acuña, M.H., Anderson, B.J., Baker, D.N., Benna, M., Gloeckler, G., et al. (2008). Mercury's magnetosphere after MESSENGER's first flyby. *science*, 321(5885), pp.85-89.

47. Slavin, J.A., Acuña, M.H., Anderson, B.J., Baker, D.N., Benna, M., Boardsen, S.A., et al. (2009). MESSENGER observations of magnetic reconnection in Mercury's magnetosphere. *science*, 324(5927), pp.606-610.

48. Stephens, G.K. & Korth, H. (2024). An empirical model for Mercury's field-aligned currents derived from MESSENGER Magnetometer data. *Journal of Geophysical Research: Space Physics*, 129(2), p.e2023JA031702.

49. Tenfjord, P., Østgaard, N., Snekvik, K., Laundal, K.M., Reistad, J.P., Haaland, S. & Milan, S.E. (2015). How the IMF By induces a By component in the closed magnetosphere and how it leads to asymmetric currents and convection patterns in the two hemispheres. *Journal of Geophysical Research: Space Physics*, 120(11), pp.9368-9384.

50. Wang, X.D., Fatemi, S., Nilsson, H., Futaana, Y., Holmström, M. & Barabash, S. (2023). Solar wind interaction with Mars: electric field morphology and source terms. *Monthly Notices of the Royal Astronomical Society*, 521(3), pp.3597-3607.

51. Winslow, R.M., Anderson, B.J., Johnson, C.L., Slavin, J.A., Korth, H., Purucker, M.E., et al. (2013). Mercury's magnetopause and bow shock from MESSENGER Magnetometer observations. *Journal of Geophysical Research: Space Physics*, 118(5), pp.2213-2227.